Article

Tailoring of Novel Azithromycin-Loaded Zinc Oxide Nanoparticles for Wound Healing

Mohammed S. Saddik [1], Mahmoud M. A. Elsayed [1,*], Mohamed A. El-Mokhtar [2], Haitham Sedky [3],
Jelan A. Abdel-Aleem [4], Ahmed M. Abu-Dief [5,6], Mostafa F. Al-Hakkani [7,8], Hazem L. Hussein [9],
Samah A. Al-Shelkamy [10], Fatma Y. Meligy [11], Ali Khames [12] and Heba A. Abou-Taleb [13]

[1] Department of Pharmaceutics and Clinical Pharmacy, Faculty of Pharmacy, Sohag University, P.O. Box 82524, Sohag 82524, Egypt; mohammed.sherif@pharm.sohag.edu.eg

[2] Department of Medical Microbiology and Immunology, Faculty of Medicine, Assiut University, Assiut 71515, Egypt; elmokhtarma@aun.edu.eg

[3] Department of Microbiology and Immunology, Faculty of Pharmacy, Assiut University, Assiut 71515, Egypt; haitham.mohamed@aun.edu.eg

[4] Department of Industrial Pharmacy, Faculty of Pharmacy, Assiut University, Assiut 71516, Egypt; Jelan.abdelrazik@pharm.aun.edu.eg

[5] Chemistry Department, College of Science, Taibah University, Madinah 42353, Saudi Arabia; amamohammed@taibahu.edu.sa

[6] Chemistry Department, Faculty of Science, Sohag University, Sohag 82524, Egypt

[7] Department of Chemistry, Faculty of Science, Al-Azhar University, Assiut Branch, Assiut 71524, Egypt; dr.mostafa.farouk.83@gmail.com

[8] Department of Chemistry, Faculty of Science, New Valley University, El-Kharja 72511, Egypt

[9] Department of Dermatology, Venereology and Andrology, Faculty of Medicine, Al-Azhar University, Assiut Branch, Assiut 71524, Egypt; Lotfyh774@gmail.com

[10] Department of Physics, Faculty of Science, New Valley University, El-Kharja 72511, Egypt; Samah.ahmed@scinv.au.edu.eg

[11] Department Histology, Faculty of Medicine, Assiut University, Assiut 71524, Egypt; Fmeligy@aun.edu.eg

[12] Department of Pharmacology and Toxicology, Faculty of Pharmacy, Sohag University, Sohag 82524, Egypt; ali_khamies@yahoo.com

[13] Department of Pharmaceutics and Industrial Pharmacy, Faculty of Pharmacy, Merit University (MUE), Sohag 82755, Egypt; Heba.ahmed@merit.edu.eg

* Correspondence: mahmoudalmenshawy@pharm.sohag.edu.eg; Tel.: +20-122-766-0470

Abstract: Skin is the largest mechanical barrier against invading pathogens. Following skin injury, the healing process immediately starts to regenerate the damaged tissues and to avoid complications that usually include colonization by pathogenic bacteria, leading to fever and sepsis, which further impairs and complicates the healing process. So, there is an urgent need to develop a novel pharmaceutical material that promotes the healing of infected wounds. The present work aimed to prepare and evaluate the efficacy of novel azithromycin-loaded zinc oxide nanoparticles (AZM-ZnONPs) in the treatment of infected wounds. The Box–Behnken design and response surface methodology were used to evaluate loading efficiency and release characteristics of the prepared NPs. The minimum inhibitory concentration (MIC) of the formulations was determined against Staphylococcus aureus and Escherichia coli. Moreover, the anti-bacterial and wound-healing activities of the AZM-loaded ZnONPs impregnated into hydroxyl propyl methylcellulose (HPMC) gel were evaluated in an excisional wound model in rats. The prepared ZnONPs were loaded with AZM by adsorption. The prepared ZnONPs were fully characterized by XRD, EDAX, SEM, TEM, and FT-IR analysis. Particle size distribution for the prepared ZnO and AZM-ZnONPs were determined and found to be 34 and 39 nm, respectively. The mechanism by which AZM adsorbed on the surface of ZnONPs was the best fit by the Freundlich model with a maximum load capacity of 160.4 mg/g. Anti-microbial studies showed that AZM-ZnONPs were more effective than other controls. Using an experimental infection model in rats, AZM-ZnONPs impregnated into HPMC gel enhanced bacterial clearance and epidermal regeneration, and stimulated tissue formation. In conclusion, AZM -loaded ZnONPs are a promising platform for effective and rapid healing of infected wounds.

1. Introduction

Wound healing is a critical process that involves four stages, including hemostasis, inflammation, proliferation, and maturation [1,2]. Any interruption of these stages will retard the repair of damaged tissues. The healing process can also become impaired and complicated because of infection by pathogenic bacteria that colonize the damaged tissues, with increasing incidence of spreading the infection and systemically leading to fever and sepsis [3]. So, there is an urgent need for the development and discovery of novel materials that cure infected wounds and accelerate the healing process.

Nanomaterials have a great intrinsic potential for preventing and treating wound infections, with multiple advantages compared with traditional treatment approaches [3,4]. Metal and metal oxide nanoparticles [5–7] exhibit remarkable antibacterial activities against different pathogens, in addition to their low toxicity profile [8,9].

ZnO is a bio-safe material that possesses multiple functions, including photo-oxidizing and photocatalysis impacts on chemical and biological species [10,11]. Additionally, its UV-blocking activity has directed its use in sunscreen preparations [12]. Many reports have shown the antibacterial activity of zinc oxide nanoparticles (ZnONPs) against both Gram-negative and Gram-positive bacteria. Furthermore, ZnONPs are considered ideal candidates for carrying pharmaceutically active molecules [13].

Several approaches can be used for the synthesis of ZnONPs as physical fragmentation and chemical, such as sol-gel, vapor condensation, amorphous crystallization, green methods, and many others [14–18].

Alternatively, AZM belongs to the macrolide group of antibiotics. This group of antibiotics selectively binds to the bacterial 50S ribosomal subunit, thereby inhibiting the vital process of protein synthesis. It is a dicationic molecule that is characterized by its ability to permeate the bacterial outer membrane of bacteria, which is an important step in overcoming bacterial self-defense [19].

Many studies have reported remarkable benefits of the adsorption of drugs on the surface of metals and metal oxide nanomaterials, such as adsorption of phenytoin on copper nanoparticles for wound healing [20] and 5-Fu on chromium nanoparticles for colorectal cancer treatment [21]. This is the first study to report on the adsorption of AZM onto the surface of ZnONPs. Considering the interesting findings of ZnONPs and AZM in the healing process of infected wounds, the major objective of our study is to explore the effect of AZM-ZnONPs for treating infected wounds. AZM-ZnONPs were characterized for morphology, FT-IR, and XRD. Moreover, AZM adsorption isotherm onto a ZnONP surface was investigated. The in vitro antibacterial activities were evaluated. Additionally, the in vivo antibacterial and wound-healing activities of AZM-loaded ZnONP-impregnated HPMC gel was also performed using an excisional wound model in rats.

## 2. Material and Methods

2.1. Employed Reagents in the Current Investigation

All the chemicals used in the current research were analytical grade and were not further purified. HPMC was used as a gelling agent and purchased from Sigma-Aldrich (St Louis, MO, USA). AZM (AZM) was used as the adsorbate and was received as a gift from El-Nile Company for Pharmaceutical Industries (Cairo, Egypt). $Zn(NO_3)_2$ $6H_2O$ (Sigma-Aldrich) was the zinc precursor, whereas sodium bicarbonate $NaHCO_3$ (98%, Alfa Aesar) was the precipitating agent, and solvents (de-ionized water) were used for washing the formed precipitate.

2.2. Methods

2.2.1. Synthesis of ZnONPs

ZnONPs were prepared by a combination of precipitation and calcination methods. One gram of zinc nitrate $Zn(NO_3)_2$ $6H_2O$ was dissolved in 30 mL bi-distilled water and magnetically stirred until the reagents were fully dissolved. After that, a drop-by-drop solution of $NaHCO_3$ (2 M) was added to the dissolved mixture with continuous stirring until pH = 7 was reached. The resulting product was further agitated for 1 h, centrifuged, and washed several times with de-ionized water before being dried at 120 °C for 12 h. The powder was ground to pass through meshes before being placed in a crucible for calcination at 800 °C for 2 h at a rate of 10 °C/min. Finally, the ZnONP powder obtained was used for further analysis (Scheme 1).
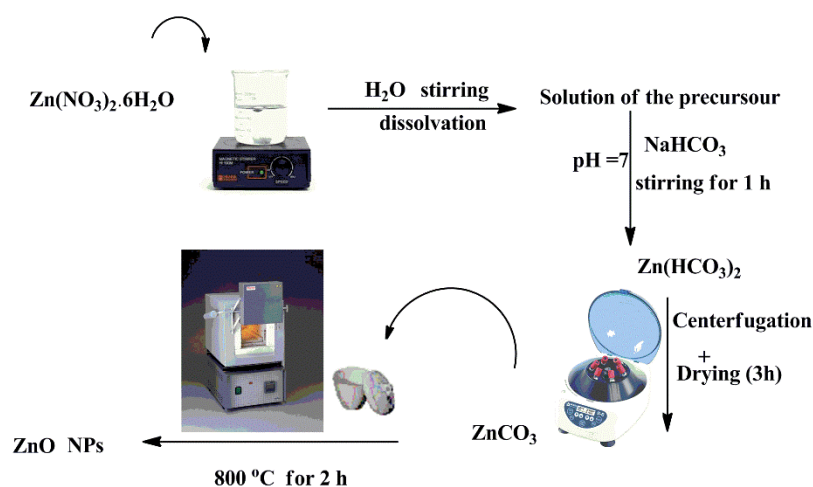
Scheme 1. Synthesis pathway for the investigated ZnONPs.

2.2.2. Adsorption of AZM by ZnONPs

In this study, the drug concentration effect on the adsorption performance was evaluated using the batch-adsorption mode. A stock solution of 1 mg/mL in absolute alcohol as a solvent of AZM was prepared. Then, serial dilutions of AZM concentration at 0.1, 0.2, 0.3, 0.4, and 0.5 mg/mL were conducted from the stock solution to determine the drug concentration that indicated the highest removal percentage. The experiments were performed in a 100 mL Erlenmeyer conical flask with a final solution volume of 40 mL with fixed stirring at 500 rpm at room temperature (25 $\pm$ 1 °C) using 100 mg ZnONPs for 5 h. Subsequently, the solution was centrifuged at 10,000 rpm and filtered via the vacuum pump using a nylon filter paper of 0.45 μm. The unbound AZM concentration was measured by the previously reported HPLC method [22]. The adsorption performance was repeated for three replicates for all experiments (as standard without ZnONPs and tested with ZnONPs) to assess the robustness of the method repeatability according to quality control and method validation guidelines [23–27]. The results were obtained as the mean of three experimental replicates. The drug removal P (%) and the adsorbed loaded amount "adsorption capacity" at equilibrium conditions, q_e (mg/g), were calculated as the equations in Table 1.

The Langmuir, Freundlich, Temkin, and D-R isotherm models were also conducted on the experimental results to determine the appropriate isothermal model as the following equations.

2.2.3. X-ray Diffraction, Scanning Electron Microscope, and Fourier Transform-Infrared (FT-IR) Analysis

The crystallographic structure and phase composition of pure ZnONPs was investigated by X-ray diffraction (XRD) (Philips X'pert MRD diffractometer, Westhorst WH121, The Netherlands). At room temperature (RT), the diffraction peaks were detected us-

ing Cu-Ka radiation (1.5418) with glancing incidence and an angle of incidence of 0.75°. All data were gathered at 2 from 10° to 80° with a step of 0.05° and a counting time of 2.5 s/step for typical powder patterns.

Table 1. Different equations of the isothermal models implemented for the investigation of the adsorption process of AZM using ZnONPs.

Equation	No.	Parameter Indications
AZM adsorbed amount [28] $q_e = (C_0 - C_e)V/M$	(1)	q_e: adsorbed amount of AZM (mg/g) C_0: initial concentrations of AZM (mg/L) C_e: equilibrium concentration of AZM (mg/L) V: volume of the AZM (mL) M: ZnONPs mass (mg)
AZM adsorption percentage [28] $P\,(\%) = (C_0 - C_e)/C_0 \times 100$	(2)	
Langmuir [29] $C_e/q_e = (1/q_L K_L) + (1/q_L)C_e$ $R_L = 1/(1 + K_L C_{max})$	(3) (4)	q_L: monolayer adsorption capacity of ZnONPs (mg/g) K_L: Langmuir energy of adsorption constant (L/mg) R_L: sensitive equilibrium parameter or separation factor C_{max}: Highest initial drug concentration in the solution (mg/L)
Freundlich [30] $log\ q_e = log\ K_F + (1/n)\ log\ C_e$	(5)	K_F: Freundlich adsorption capacity of ZnONPs (mg/g) n: Freundlich constant characteristics of the system, indicating the adsorption intensity
Temkin [31] $q_e = B_T\ ln\ A_T + B_T\ ln\ C_e$ $b_T = RT/B_T$	(6) (7)	A_T: binding constant (L/mg), related to the maximum binding energy B_T: Temkin adsorption constant (KJ/mol), related to the sorption heat R: gas constant (8.314 J/mol K) T: absolute temperature at 298 K b_T: adsorption process constant
D-R [28] $ln\ q_e = ln\ q_m - \beta\varepsilon^2$ $\varepsilon = RT\ (1 + 1/C_e)$ $E_D = (-2\beta)^{-1/2}$	(8) (9) (10)	q_m: D-R adsorption capacity of ZnONPs (mg/g) β: coefficient related to the mean free energy (mol^2 KJ^{-2}) ε: Polanyi potential E_D: adsorption energy per molecule of the AZM adsorbate when it is transferred to the surface of the solid ZnONPs from infinity in the solution (kJ/mol)

The chemical composition of the samples was examined using a scanning electron microscope (SEM) (model: JEOL-6610VL, Tokyo, Japan) fitted with an X-Max Silicon Drift Detector for energy dispersive X-ray spectroscopy (EDXS, Oxford, UK) analysis and a 20 kV accelerating voltage [32,33]. The size of the nanoparticles in the samples was measured using transmission electron microscopy (TEM) (model: JEOL-JEM-2100F Tokyo, Japan) with a field emission gun and a 200 kV accelerating voltage (FEG). The Fourier transform-infrared (FT-IR, Perkin-Elmer, Norwalk, CT, USA) analysis of ZnO and AZM-ZnONPs was collected at RT using the KBr pellet disc technique in the wavelength range of 400–4000 cm^{-1}.

2.2.4. In Vitro Drug-Release Study

In vitro release of AZM from the formulated ZnONPs was performed using the dialysis release method as previously reported [34–36] with some modification. Two mL of AZM-loaded ZnONP suspension containing 0.2 mg of AZM was placed on a dialysis membrane (MW cut off 12,000 Da) firmly stretched over one end of a glass cylindrical tube (3 cm^2 diameter). The tube was then immersed in a 100 mL beaker containing 50 mL phosphate buffer saline (PBS) at pH 7.4 and placed in a thermostatic water bath at 37 °C and shaken at 100 rpm. At predetermined time intervals, 5 mL of sample were withdrawn and replaced by an equal volume of PBS to maintain the sink condition. The amount of AZM released was determined by HPLC as previously reported.

2.2.5. Experimental Design

The formulation characteristics of AZM-ZnONPs were examined and optimized using a Box–Behnken experimental design (BBD) for the maximum LE percentage and

rapid drug delivery after 1 and 3 h [21,37–41]. In circumstances involving more than two dependent variables, this design was chosen since it necessitates fewer treatment combinations than other designs [42–44]. The BBD is also ratable and has statistical "missing corners," which can help the experimenter avoid combination factor excesses. In such instances, this characteristic prevents data loss [45]. AZM-ZnONPs were prepared using a three-factor, three-level design. AZM concentration (X_1), ZnONP weight (X_2), and temperature were the three independent formulation factors investigated during the study (X_3). Table 1 shows the variables that were chosen, with their real and coded values according to the plan. AZM-ZnONP formulae were developed based on this design (D1–D15). In the preceding design, three levels of AZM concentration were used: 0.25, 0.5, and 0.75%, signified by the numbers 1, 0, and +1, respectively. The weights of ZnONPs applied were 300, 400, and 500 mg, which corresponded to the values −1, 0, and +1, respectively. Eventually, the reflux temperature was set to $20 \pm 1\,^\circ\mathrm{C}$, $25 \pm 1\,^\circ\mathrm{C}$, and $30 \pm 1\,^\circ\mathrm{C}$, expressed by the numbers −1, 0, and +1, respectively. The loading efficiency % (Y_1), release in 1 h (Y_2), and release in 3 h (Y_3) were chosen as the dependent variables to be examined for the produced AZM-ZnONPs.

2.2.6. Preparation of AZM, Plain ZnONPs, and AZM-Loaded ZnONP-Impregnated HPMC Gels

HPMC was selected as the gelling agent at a concentration level of 2.5% (*w/v*) in accordance with a previously reported procedure [20]. Briefly, HPMC gel was prepared by dispersing the polymer in preheated distilled water (80 °C). Then, the prepared dispersion was stirred at 1000 rpm using a magnetic stirrer (Thermo Fisher Scientific, NJ, USA) until a homogeneous mixture was attained. To the prepared gel base, accurate amounts of AZM (0.01% *w/w*), AZM-loaded ZnONPs (0.0623% *w/w*), and plain ZnONPs (0.0623% *w/w*) were added and stirring was continued until a homogenous distribution was obtained. Finally, the prepared gels were kept in the refrigerator at 4 °C until the next use.

2.2.7. In Vitro Antibacterial Activity

The in vitro antibacterial activity of the AZM-ZnONPs was initially tested using the agar diffusion method against clinical isolates of methicillin-resistant *Staphylococcus aureus* (MRSA) and *Escherichia coli* (*E. coli*). A freshly prepared bacterial suspension of 0.5 McFarland turbidity was inoculated on the surface of Mueller–Hinton agar plates and 1 cm wells were prepared using a cork borer. Agar was removed from the wells and AZM, ZnO, AZM-ZnONPs, and saline solution (negative control) were added to the formed wells. Plates were incubated at 37 °C overnight and the diameters of the inhibition zones were recorded [46,47].

2.2.8. Determination of the Minimal Inhibitory Concentration (MIC)

The MICs of the AZM, ZnO, and AZM-loaded ZnONPs were determined against the clinical MRSA and *E. coli* isolates using the broth dilution technique [48]. Firstly, different formulations were serially diluted in a 96-well plate in Mueller–Hinton broth starting at a concentration of 200 µg/mL. Then, the bacterial suspension was added to each well, the plate was incubated at 37 °C for 24 h, and the MICs were determined based on the determination of the lowest concentration showing visualized growth inhibition.

2.2.9. In Vivo Antibacterial and Wound-Healing Efficacy

The in vivo antimicrobial and wound-healing activities of AZM and AZM-ZnONPs were tested in an excision wound model in rats [49]. Rats were housed at room temperature ($25 \pm 1\,^\circ\mathrm{C}$) and subjected to light/dark cycles. Experiments were conducted in accordance with the internationally accepted Guidelines for the Care and Use of Laboratory Animals [50] and the protocol was approved by the Faculty of Pharmacy's Ethics Committee (ES06/2020). Briefly, 20 albino rats were divided into four groups, each containing five rats. After intraperitoneal thiopental anesthesia, the skin on the dorsal surfaces was shaved and

a 1 cm^2 circular incision was carefully made using sharp sterile scissors. Five minutes later, the wound was inoculated with 100 μL of MRSA suspension containing approximately 10^8 colony-forming units (CFU). After 24 h of wound inoculation, groups I, II, and III received treatment two times daily with AZM, ZnO, and AZM-ZnONPs impregnated in 2.5% HPMC gel preparations, respectively, whereas the wounds of non-treated control group IV received blank non-medicated HPMC gel (untreated control group). On days 1, 3, and 7 after wounding, the wounds were photographed and a swab was obtained to determine the bacterial load. The bacterial swabs were spread on the surface of mannitol salt agar and incubated at 37 °C for 24 h to determine the number of CFUs. In addition, for the duration of 10 days after infection, the wound area and wound contraction were determined daily to evaluate the effect of the treatment on the wound-healing process, as previously described [49,51].

2.2.10. Histological Evaluation

Skin specimens were fixed in 10% formalin, dehydrated, embedded in paraffin, and then were cut into 5 μm sections. Staining with hematoxylin and eosin (H&E) stain was done to determine the general skin structure and histological changes in the epidermis and dermis. A group of uninjured rats (negative control group) was included in the study to elucidate the normal skin characteristics and for comparison purposes.

Masson's trichrome dye was used to see the collagen fibers. Using computerized image analyzer system software (Leica Q 500 MCO; Leica, Wetzlar, Germany) attached to a camera with a Leica universal microscope, the thickness of the epidermis was calculated on H&E-stained sections. The measurements were done using a ×40 objective lens. Each group had five serial sections taken. Measurements were taken in six nonoverlapping fields in each region. The epidermal thicknesses were measured in μm using the arbitrary distance technique, which involves drawing a straight line from the foundation membrane to the epidermis' top limit [52,53]. The average of six separate area measurements was calculated. Additionally, the mean percent of the area of collagen fibers in the dermis was determined using Masson's trichrome. The measurements were done in six nonoverlapping fields from five different sections in each group with a ×10 objective lens.

3. Results and Discussion

3.1. FT-IR Analysis

The chemical bonding and purity of our analyzed materials were further checked using FT-IR analysis. Figure 1A and Table 2 depict the raw FTIR-transmittance spectra of pure ZnO, AZM, and AZM-ZnONPs in the range of 400–4000 cm^{-1} at RT. The characteristic Zn–O stretching mode for wurtzite ZnO was identified in the investigated ZnO and AZM-ZnONPs in the far infrared region at wave numbers between 430 and 445 cm^{-1}. These stretching modes below 500 cm^{-1} are suggestive of the successful production of ZnONPs [54]. The O-C-O bending mode of carbonate was ascribed to the band centered at 877–880 cm^{-1}, which is commonly found when FT-IR samples are examined without vacuum [55]. The O-H stretching and O-H-O bending vibration modes of surface-adsorbed molecules of water were ascribed to the substantial transmittance bands at 3415–3415 cm^{-1} and 1625–1664 cm^{-1}, respectively [56].

Various AZM characteristic bands could be identified in the spectra acquired straight from the solid standard, as shown in Figure 1A. The main bands identified were (i) bands associated with the axial stretching and bending of C-H of the methyl groups, which were found in the ranges of 2966–2985 cm^{-1} and 1367–1374 cm^{-1}, respectively [57,58]; (ii) the sharp and powerful band at 1710–1722 cm^{-1}, which could be attributed to the axial stretching of the lactone's C=O group; and (iii) other notable bands in the spectra, including those found in the 1130–1225 cm^{-1} region, which emerged due to absorption related to C-O axial stretching [59].
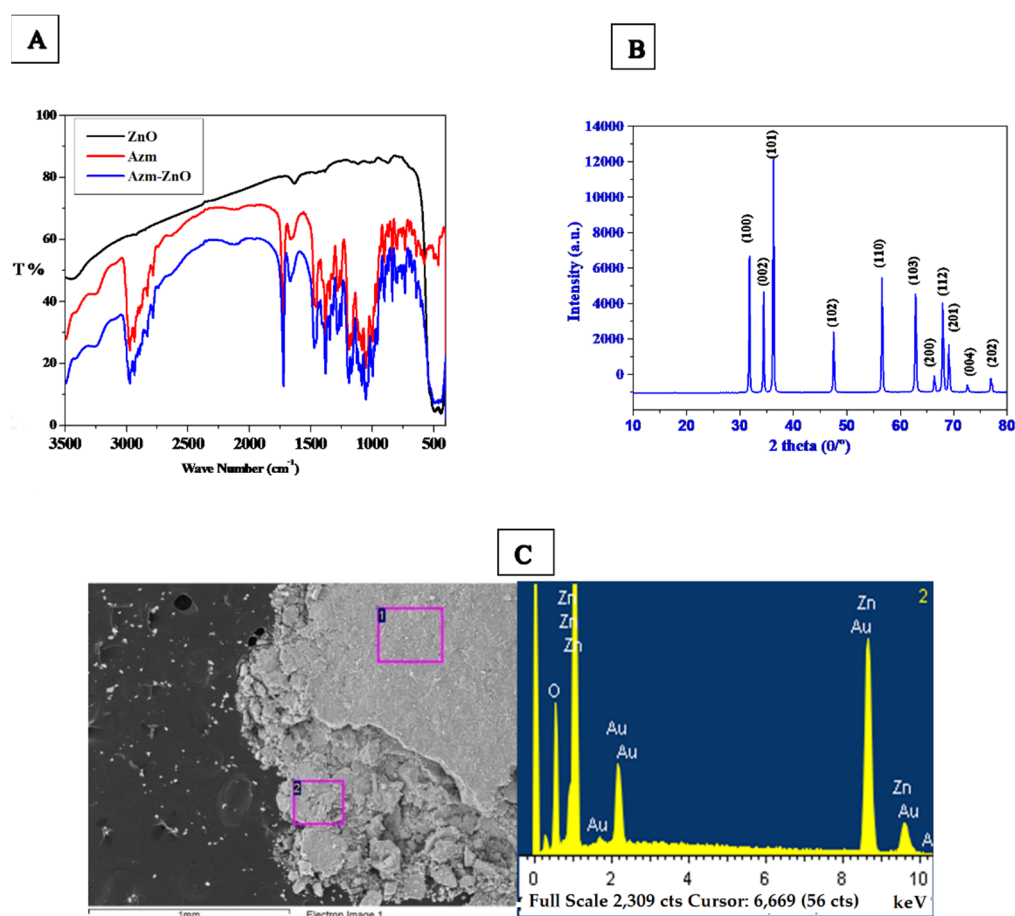
Figure 1. (**A**) FT-IR spectra of ZnONPs, AZM, and AZM-ZnO nanoparticles; (**B**) typical XRD patterns of the prepared ZnO nanoparticles (note: The numbers above the peaks correspond to the miller index (hkl) values of hexagonal ZnO); (**C**) EDXS spectra of the investigated ZnONPs.

Table 2. FT-IR spectra data of ZnONPs, AZM, and AZM-ZnO nanoparticles.

ZnONPs	AZM	AZM-ZnO Nanoparticles	Band Assignment
3462	3424	3415	Stretching of OH/H_2O
	3247	3268	Stretching of NH
	2966	2985	Stretching of aliphatic CH
	1710	1722	Stretching C=O
1625	1655	1664	O-H-O bending vibration modes
	1367	1374	Bending aliphatic -CH
445		435	Vibrational Zn-O

3.2. XRD Analysis

XRD analysis was used to analyze the phase crystalline nature and purity of the produced ZnO powder sample. The XRD patterns of ZnONPs are shown in Figure 1B and XRD data in Table S1. The sample showed strong and sharp diffraction peaks, suggesting that the ZnONPs crystallized to a great degree. The hexagonal (wurtzite) phase of crystalline ZnO, the space group P63mc with lattice constants a = 3.253 and c = 5.213, (Standard JCPDS file No. 76-0704), could be well indexed in the XRD spectra; no other supplementary crystalline phases linked to contaminants were detected by XRD, showing a high wurtzite phase purity of the as-synthesized ZnONPs. Furthermore, the largest peak intensity of the ZnONP sample was at $2\theta = 36.275°$, which was associated with 101 Miller indices associated with the wurtzite ZnO phase.

The average crystallite size (D_v) of the ZnO sample was estimated using the well-known Debye–Scherer formula [60–62]:

$$D_v = \frac{0.94\lambda}{(FWHM)\cos\theta} \tag{11}$$

where λ is the wavelength of the x-radiation source (i.e., λ = 1.5418 Å), FWHM is the full width at half maximum in radians along the 120 plane, and θ is the diffracted Bragg angle. The crystallite size determined by XRD analysis (38 nm) matched the usual particle size determined by TEM examination (39 nm).

3.3. EDAX Analysis

To investigate the elemental and compositional stoichiometry properties of the investigated ZnO sample, the chemical composition ZnONP sample was analyzed using energy-dispersive X-ray spectroscopy (EDXS). Figure 1C indicates the typical EDAX spectra of pure and mixed ZnO nanostructure samples. It is clear from the observed EDAX spectra that the prepared powder sample was composed of zinc (Zn) and oxygen (O) without any impurities, which confirmed the high purity of the prepared powder sample.

3.4. Microstructural Studies by SEM and TEM Analysis

SEM and TEM investigation confirmed that the ZnONP sample had a sphere-like morphology with monodispersion nanoparticles. Typical SEM and TEM micrographs of ZnONPs and AZM-ZnO samples clearly demonstrated the large aggregates of near spherical shapes with different particle sizes of the as-synthesized samples, as shown in Figure 2. It is clear that the size and the morphology of the particles were little affected by the adsorption of AZM on ZnONPs. In addition, Figure 2D,F show the corresponding diameter distribution histogram of the ZnONP and AZM-ZnO samples estimated by Image J software and Excel calculation [63–65]. From TEM analysis, the calculated mean particle sizes matched well with the values that were obtained from the XRD analysis.

3.5. Adsorption of AZM by ZnONPs

The effect of drug concentration on the removal performance is shown in Figure 3. As the drug concentration increased from 100 to 200 mg/L, the drug removal decreased from 78.0 to 66.2%. The decrease in the removal depended on the drug concentration and empty sites of the adsorbent. At high concentrations of the drug, the drug adsorbed on the empty sites of the adsorbent until a saturation state was achieved [20] (Scheme 2). When the drug concentration continued to increase from 300 to 500 mg/L, the removal percentage slightly decreased from 59.0 to 55.9%. Nevertheless, the decrease can be neglected. Moreover, the drug removal percentage depending on the drug concentration showed a constant trend after a drug concentration of 300 mg/L.

Adsorption Isotherm Studies

The four different isotherm models were used to determine the most suitable model for design purposes. The isotherm calculations were done as shown in Table 3.

According to the R^2 values given in Table 3 and Figure 4, the most fitted isotherm model was determined to be the Freundlich isotherm. According to the Freundlich model, the adsorbent was heterogeneous on the surface with a multilayer adsorption capacity. We could also estimate some important parameters of the adsorption study according to the manifested data from different implemented isothermal models, such as the following.

The isotherm adsorption process of AZM on the ZnONP surface could be arranged as follows: Freundlich > Temkin > Langmuir > D-R model using the R^2 values as an indication parameter.
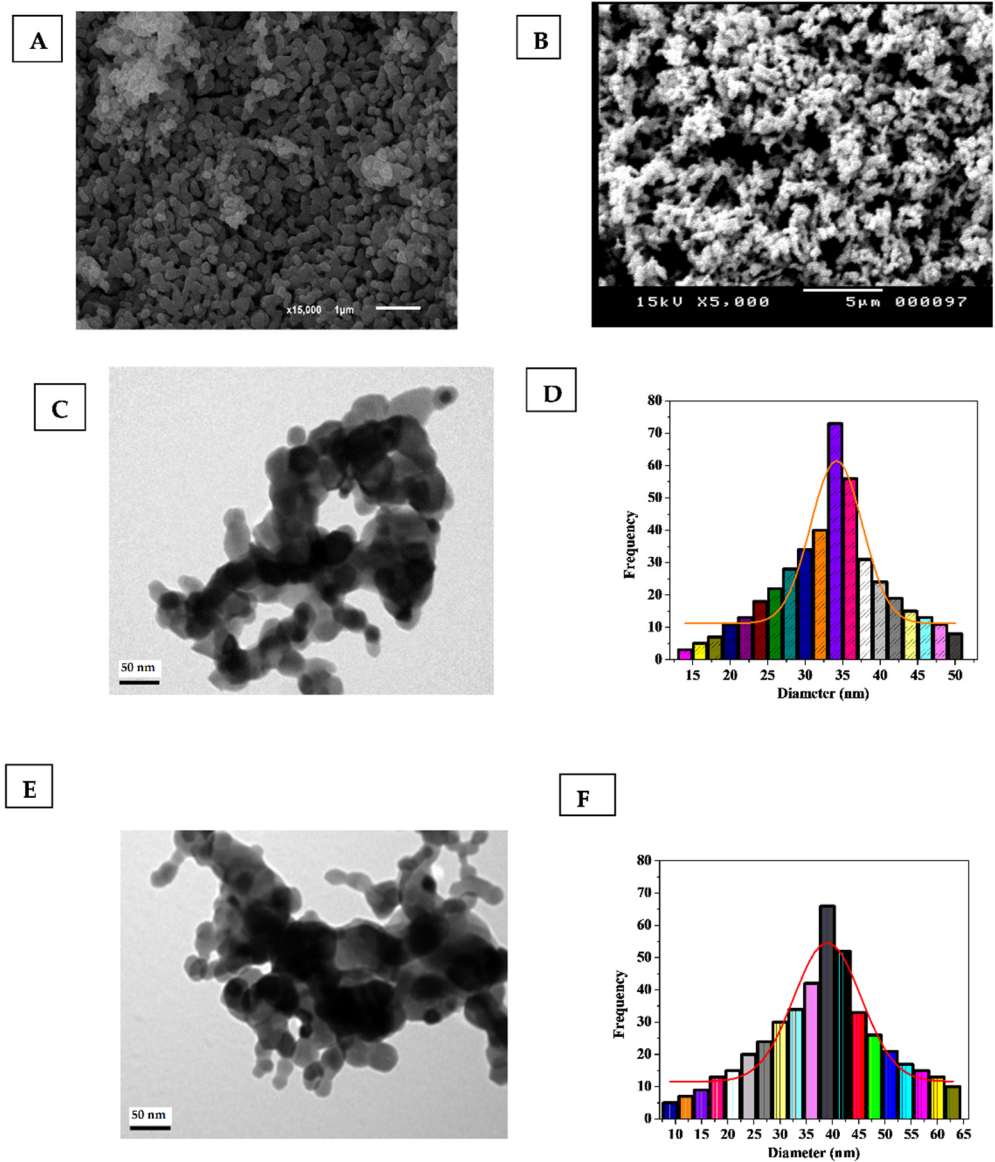
Figure 2. SEM image of (**A**) ZnONPs and (**B**) AZM-ZnONPs; TEM images of (**C**) ZnONPs and (**E**) AZM-ZnONPs and their particle size distribution in (**D**,**F**), respectively.
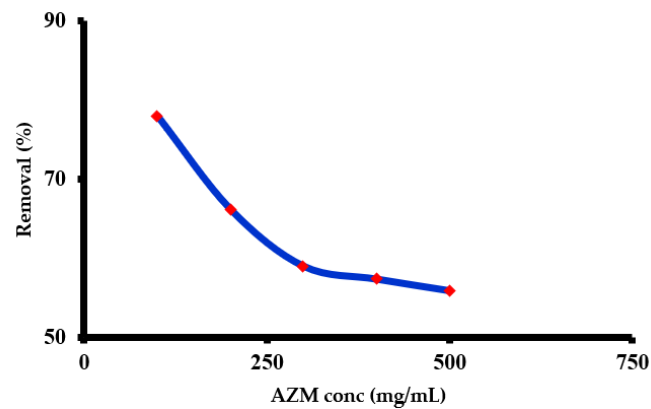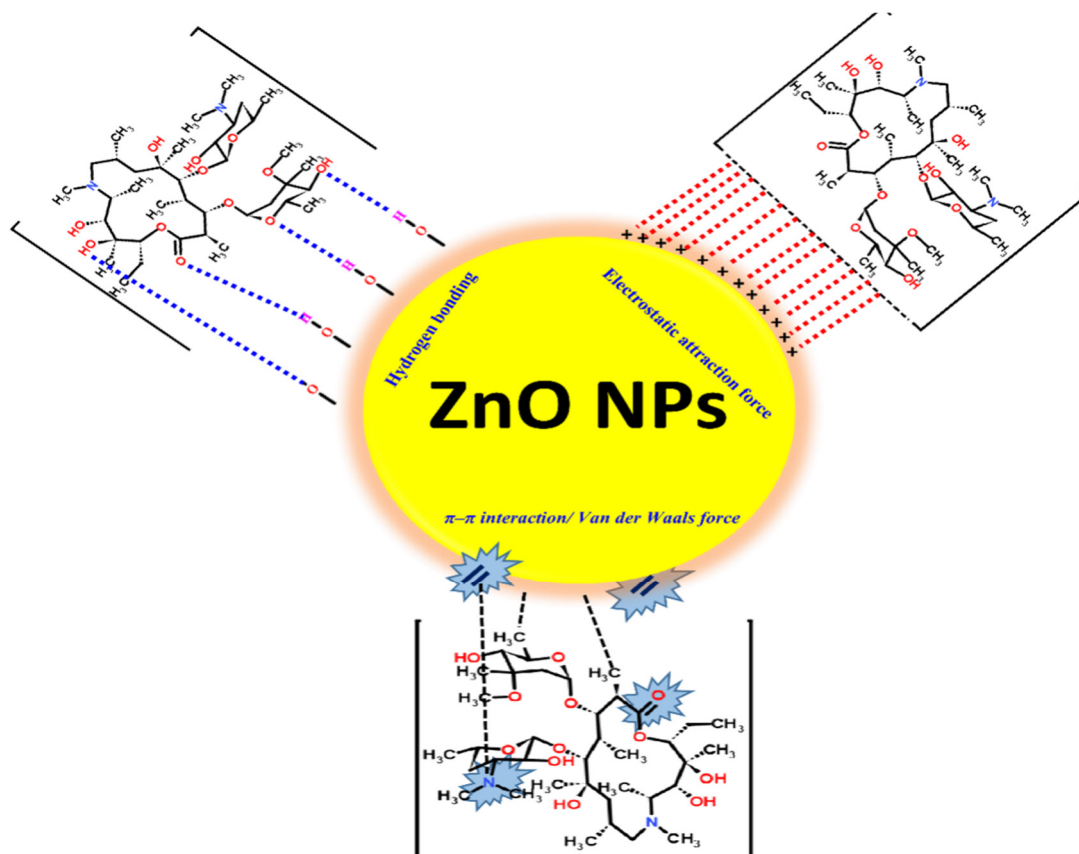
Figure 3. Removal performance of the AZM at different concentrations via ZnONPs.

Scheme 2. AZM-ZnONP binding mechanism probabilities.

Table 3. Isotherm models of the adsorption of AZM onto the ZnONPs.

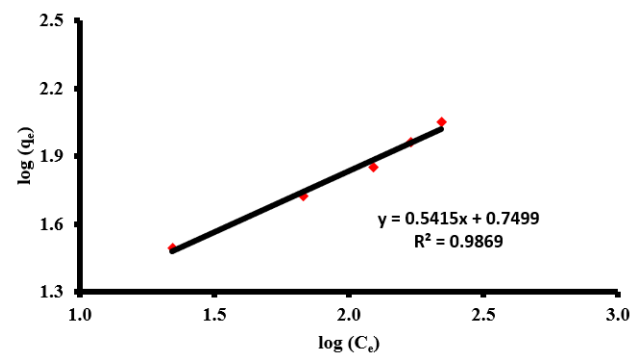| Item	Isothermal Models			
	Langmuir	**Freundlich**	**Temkin**	**D-R**
R^2	0.8918	0.9869	0.9114	0.7595
	$q_L = 160.44$	$n = 1.847$	$A_T = 0.095$	$q_m = 82.9$
Model parameter	$k_L = 0.008$	$1/n = 0.541$	$B_T = 32.9$	$\beta = -8.39 \times 10^{-5}$
	$R_L = 0.196$	$k_F = 5.6$	$b_T = 74.06$	$E_D = 77.2$

Figure 4. Freundlich isotherm model of the adsorption of AZM via ZnONPs.

The Freundlich model indicated the type of adsorption where it was found to be desirable and favored according to the n parameter that was found (1.847) between 1 and 10. The 1/n value was also found to be less than the unit, at 0.541, which revealed that adsorption follows a heterogeneity pattern at the ZnONP surface. According

to the Langmuir model, q_L (160.4 mg/g) was found to be more than the experimental q_e (111.7 mg/g). The adsorption process was also found to be favorable according to the R_L, where R_L was more than 0 and also less than the unit and the actual value was found to be 0.196. As for the Temkin model, the heating of the adsorption process of b_T (74.06 kJ/mol) was found to be less than 80 kJ/mol, which means the adsorption was physisorptive in nature [20,28]. The D-R isothermal model was also investigated and gave us an indication about the average of the adsorption energy (E_D) for each AZM molecule that adsorbed using ZnONPs. It was found to be 77.2. Since it was less than 80, it is indicates that the adsorption could be expressed as a physisorption type [66].

3.6. Drug-Loading Efficiency on ZnONPs (LE%)

Table 4 shows the impact of selected variables on LE percentage and drug release after 1 and 3 h. In terms of AZM concentration, the determined theoretical drug content value for D1, D5, and D12 was 20%, whereas it was 33.33% for D2, D3, D7, D8, D9, D13, and 14 and 42.85% for D4, D10, D11, and D15. Using the ANOVA test, the impact of increasing the AZM concentration on the LE percentage was examined for each AZM concentration, ZnONP weight, and temperature. The LE percentage ranged from $50.07 \pm 1.93\%$ to $87.11 \pm 3.53\%$, depending on the AZM concentration, ZnONP weight, and temperature. The fitted LE percentage model regression equation is [38,43]:

$$Y_1 = 74.55 + 7.36\,X_1 + 6.62\,X_2 - 5.14\,X_3 - 1.19\,X_1^2 - 1.47\,X_2^2 + 5.22\,X_3^2 - 2.32\,X_1X_2 + 1.66\,X_1X_3 - 0.44\,X_2X_3 \quad (12)$$

Table 4. Observed values of responses for AZM–zinc oxide nanoparticles (AZM-ZnONPs).

Formula No.	Variable Level in a Coded Form			LE%	Cumulative Percentage Released	
	X_1 AZMConc.	X_2 ZnONP Weight	X_3 Temperature	Y_1 LE %	Y_2 Rel 1 h	Y_3 Rel 3 h
D1	−1	−1	0	50.07 ± 1.93	15.46 ± 1.38	47.53 ± 1.66
D2	0	−1	−1	70.44 ± 2.98	22.42 ± 2.03	65.44 ± 2.71
D3	0	−1	1	62.31 ± 1.73	19.75 ± 1.97	54.65 ± 1.92
D4	1	−1	0	69.72 ± 2.78	21.47 ± 1.85	64.20 ± 2.33
D5	−1	0	−1	75.25 ± 2.21	20.67 ± 1.58	61.19 ± 2.94
D6	−1	0	1	62.42 ± 3.15	18.43 ± 1.74	53.54 ± 1.86
D7	0	0	0	69.13 ± 2.26	28.90 ± 1.95	72.87 ± 2.65
D8	0	0	0	78.54 ± 3.12	23.50 ± 1.34	69.15 ± 2.84
D9	0	0	0	75.99 ± 2.11	30.89 ± 1.73	77.16 ± 2.96
D10	1	0	−1	87.11 ± 3.53	28.17 ± 1.33	76.76 ± 2.34
D11	1	0	1	76.81 ± 3.57	26.68 ± 1.87	70.40 ± 2.33
D12	−1	1	0	69.33 ± 2.39	20.01 ± 1.56	56.24 ± 1.93
D13	0	1	−1	81.89 ± 2.81	27.97 ± 1.24	75.23 ± 2.75
D14	0	1	1	71.98 ± 3.23	17.59 ± 1.96	54.05 ± 2.54
D15	1	1	0	82.34 ± 2.52	19.17 ± 1.49	60.35 ± 2.63

At confidence levels of 90% and higher, there was a statistically significant correlation between the variables since the *p*-value in the ANOVA table was less than 0.1 [44]. According to the R-squared value, the model (as fitted) accounted for 94.21% of the variation in AZM concentrations. The output, on the other hand, provided the results of using a multiple linear regression model to explain the association between ZnONP weight and LE percentage. At the 90% confidence level, there was a statistically significant link between the variables since the *p*-value was less than 0.1. According to the R-squared value, the model (as fitted) explained 83.80% of the variation in ZnONPs weight. Despite the drop in LE% with increasing temperature, the temperature had no significant influence on LE% since the *p*-value was more than 0.1.

With a fixed ZnONP weight and temperature, the LE percentage rose from 50.07 ± 1.93 to $69.72 \pm 2.78\%$ and from 69.33 ± 2.39 to $82.34 \pm 2.52\%$ for lower and higher AZM concentrations, respectively (Figure 5). Because more of the drug was adsorbed and assimilated on the surface of ZnONPs with high AZM concentrations, LE% improved with higher AZM levels. The % drug incorporation was studied using a linear connection between the two variables. The two key stages in the synthesis of AZM-ZnONPs were the production of stable ZnONPs and the subsequent adsorption of AZM on the surface of the ZnONPs. These two procedures had a significant impact on the size and LE percentage of nanoparticles produced.
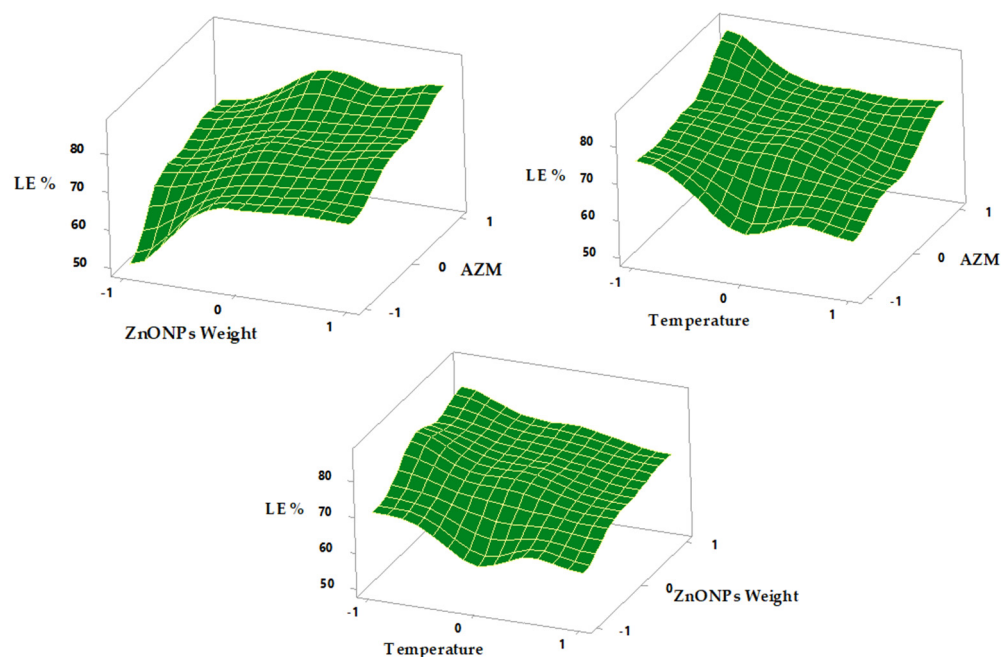
Figure 5. Surface plot effects of different formulation factors on LE%.

With a fixed AZM concentration and temperature, LE% increased from 50.07 ± 1.93 to $69.33 \pm 2.39\%$ and from 70.44 ± 2.98 to $81.89 \pm 2.81\%$ at lower and higher ZnONP weights, respectively (Table 4). The surface area available for drug loading grew as the weight of the ZnONPs rose. Because of the increased surface area, more drugs could be adsorbed on the nanoparticles' surface.

The temperature employed during nanoparticle manufacturing affected the LE% of the drug; as the temperature increased, the LE% decreased. Because the drug-adsorption process on the surface of the ZnONPs decreased as the temperature of the AZM with the ZnONP reflux process increased, these results were expected [59]. The major goal of the temperature impact study was to find the optimal reflux temperature that would result in a greater LE percentage. With a steady AZM concentration and ZnONP weight, the LE percentage fell from 70.44 ± 2.98 to $62.31 \pm 1.73\%$ (D2, D3) and from 75.25 ± 2.21 to $62.42 \pm 3.15\%$ (D5, D6) at lower and higher temperatures (Table 4), respectively. All of these findings suggest that a lower temperature (20 ± 1 °C, -1) should be employed to get larger LE% values.

3.7. In Vitro Release Study of AZM-ZnONPs

The outputs of the correlation between AZM concentration, ZnONP weight, and temperature with the percentage drug released after 1 and 3 h is shown in regression Equations (13) and (14), respectively.

$$Y_2 = 27.76 + 2.62\,X_1 + 0.70\,X_2 - 2.10\,X_3 - 3.59\,X_1{}^2 - 2.31\,X_2{}^2 - 0.69\,X_3{}^2 - 1.71\,X_1X_2 + 0.19\,X_1X_3 - 1.93\,X_2X_3 \qquad (13)$$

$$Y_3 = 73.06 + 6.65\ X_1 + 1.76\ X_2 - 5.75\ X_3 - 5.35\ X_1{}^2 - 6{,}43\ X_2{}^2 - 1.16\ X_3{}^2 - 3.14\ X_1X_2 + 0.32\ X_1X_3 - 2.60\ X_2X_3 \qquad (14)$$

After 1 and 3 h, the AZM concentration, as well as the ZnONP weight, had a significant influence on drug release (*p*-value = 0.1). The fraction of drugs released rose as their levels rose. The temperature had no influence on drug release, in contrast to its effect on the LE percentage.

The response surface plots of the in vitro release of AZM from its ZnONPs are shown in Table 4 and Figures 6 and 7. The in vitro release of AZM from formulas D1, D2, D3, and D4 employing ZnONPs (X_2) at a constant level (-1) with varied AZM concentrations (X_1) was 0.25% for D1, 0.5% for D2 and D3, and 0.75% for D4 (X_2).
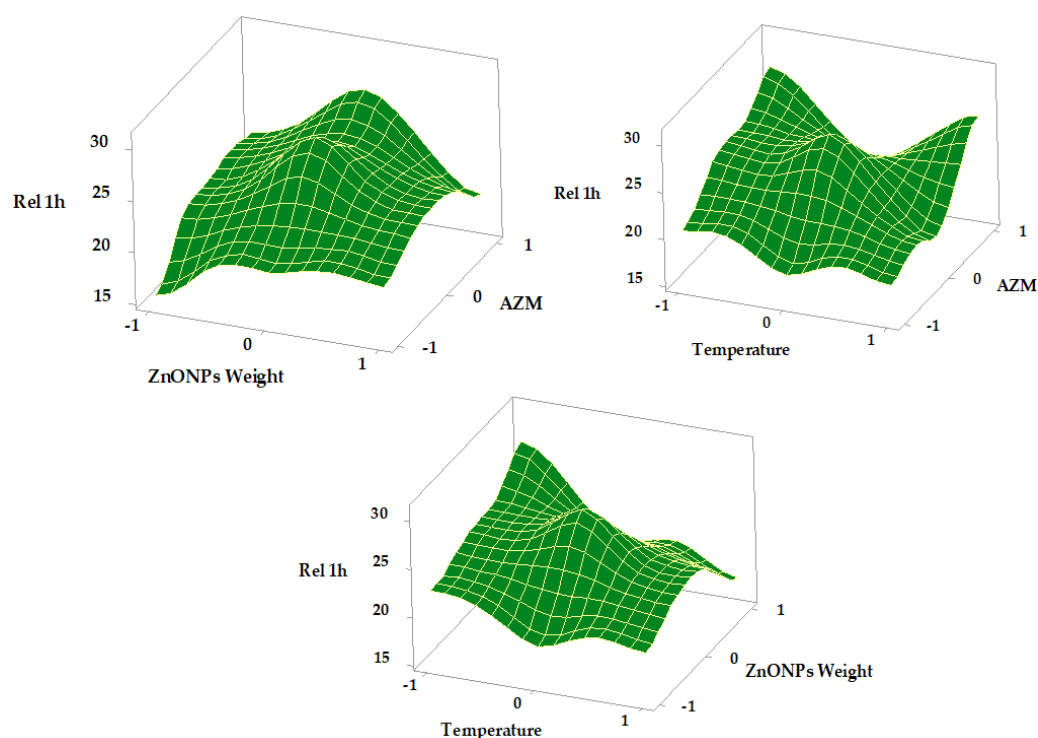
Figure 6. Surface plot effects of different formulation factors on release after 1 h.

At the completion of one hour, the highest and minimum percentages discharged were found to be 22.42 ± 1.38 and 15.46 ± 1.38%, respectively (Y_2). After 3 h (Y_3) of dissolution, the maximum and minimum in vitro releases were 65.44 ± 2.72 and 47.53 ± 1.66%, respectively. In terms of in vitro release within 3 h, the formulae investigated can be ranked as follows: D2 > D4 > D3 > D1 in descending order.

Table 4 shows the summary of in vitro AZM release from ZnONPs using formulae D5, D6, D7, D8, D9, D10, and D11 employing constant ZnONP weight (X_2) at the medium level (0), variable temperature levels (range from -1 to +1), and various different AZM concentrations (X_1).

At the end of one hour, the highest and minimum percentages released were 30.89 ± 1.73 and 18.43 ± 1.74% (Y_2), respectively. After 3 h of dissolution (Y_3), the maximum and minimum in vitro release were determined to be 77.16 ± 2.96 and 53.54 ± 1.86%, respectively.

The release of AZM from ZnONPs with formulae D12, D13, D14, and D15 in vitro was investigated using constant ZnONP weight (X_1) at the medium level (0), variable temperature levels (ranging from -1 to +1), and various different AZM concentrations (X_1).
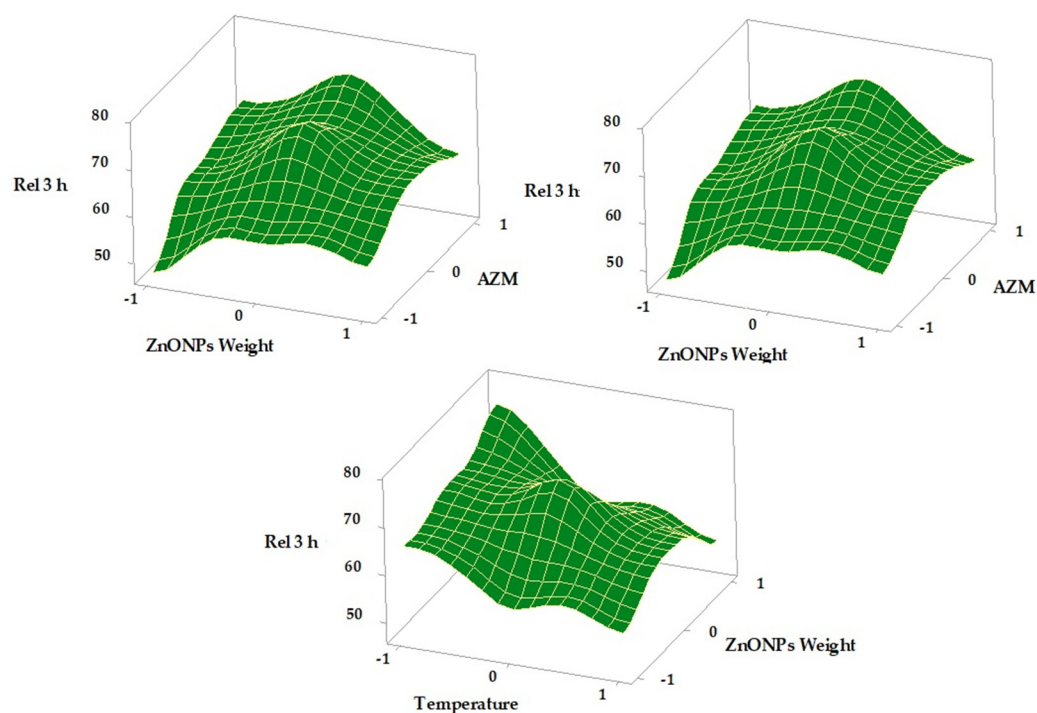
Figure 7. Surface plot effects of different formulation factors on release after 3 h.

Equations (13) and (14) show that the weight of ZnONP had a considerable favorable influence on drug release after 1 and 3 h in different formulations (9). At constant (X_1) and (X_3) (0, −1), the percentage of AZM released at the end of 3 h (Y_2) was 65.44 ± 2.71 and 75.23 ± 2.75% (D2, D13) at lower and higher ZnONPs weights, respectively.

All of these findings show that raising the AZM concentration had a substantial impact on drug release. These findings are linked to the ease with which AZM can be released since the drug was adsorbed on the surface of ZnONPs and a larger amount of the drug was accessible for release. The difficulties of desorption of AZM from ZnONPs in the release-medium environment, as well as the nature of the produced AZM-ZnONP combination, might explain these results. AZM desorbs quickly at an alkaline pH, and the amount released increased considerably due to the basic composition of the AZM and ZnONPs, which permitted more of the drug to be accessible for absorption sites. In a study by Zora Rukavina et al. [67], controlled-release AZM liposomes exhibited a sustained drug-release pattern after an initial burst release.

The weight of ZnONPs had an inverse relationship with the percentage of drugs released. These findings are indicative of the fact that when the NP weight increased, the surface area of ZnONPs increased, allowing more medication to be adsorbed on the surface of the monolayer pattern. This AZM monolayer adhesion had a deleterious impact on drug release from the ZnONP surface. The quantity of drug adsorbed in a multilayer pattern on the surface of ZnONPs, which made it more easily released because of attachment forces, decreased whenever the ZnONP weight was lowered [27,68].

Temperature showed no impact on AZM release after 1 and 3 h, in contrast to the LE percentage [42,69]. The findings of the LE percentage on in vitro release after 1 and 3 h suggest that the best AZM-ZnONPs formula should be made with a high AZM concentration (+1, 0.75%), a medium ZnONP weight (0, 500 mg), and a low temperature (−1, 20 ± 1 °C). The optimum formula was D9, according to the rank order of all formulas (considering the greater LE percentage and Rel. 1 and 3 h), and was selected for further in vivo studies.

3.8. In Vitro and In Vivo Antibacterial Activities

To evaluate the antibacterial activity of the preparations, the agar diffusion method was performed. The mean inhibition zone diameters were related to the free formulation of AZM.

A concentration of 100 µg/mL of free AZM produced about 13 ± 3 mm and 9.5 ± 2 mm against MRSA and *E. coli*, respectively. However, the same concentration of AZM-ZnONPs produced 20 ± 4 mm and 14 ± 3 mm against MRSA and *E. coli*, respectively, pointing to a higher antibacterial effect. In addition, MIC of the free drug and nano formulation was determined. The lowest inhibitory concentration of AZM was significantly reduced from 20 µg/mL to 10 µg/mL and from 32 µg/mL to 20 µg/mL in the AZM-ZnONPs against both the Gram-positive MRSA and the Gram-negative *E. coli*, respectively (Figure 8).
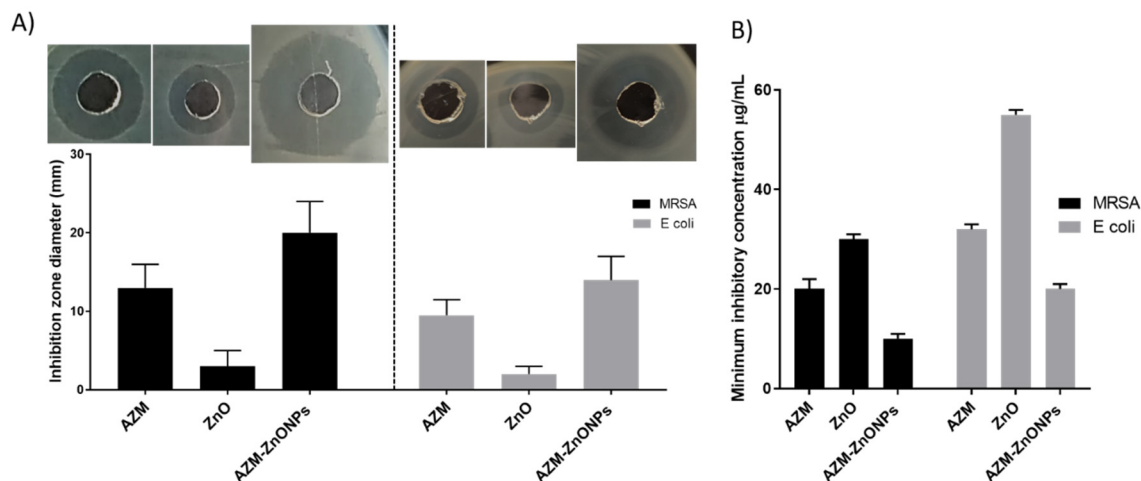
Figure 8. Azithromycin-loaded zinc oxide nanoparticles have superior anti-bacterial activities. (**A**) shows the mean inhibition zone diameters induced by azithromycin (AZM), zinc oxide (ZnO), and azithromycin-loaded zinc oxide nanoparticles (AZM-ZnONPs) in agar plates inoculated by MRSA and *E. coli,* and a representative figure of each treatment. (**B**) shows the minimum inhibitory concentrations (MIC) of AZM, ZnO, and AZM-loaded ZnONPs against MRSA and *E. coli*. Data are shown as mean $\pm$ standard deviation of 3 experiments.

To evaluate the in vivo anti-microbial and wound-healing characteristics of the formulations, different groups of wounded rats received daily treatment regimens of AZM (Group I), ZnO (Group II), or AZM-ZnONPs (Group III) and were compared with Group IV, which received a non-medicated gel. To visually elucidate the effect of AZM-ZnONP treatment, different groups of treated animals were photographed at 1, 3, and 7 days post infection (Figure 9A). Group III exhibited faster wound closure compared to other groups that received the other treatments, as demonstrated by the higher level of wound contraction percentage. Group III showed better skin appearance and normal hair growth compared to other treated rats or the control group IV, which showed a dramatic progression of the wound area with reduced healing.

Furthermore, bacterial counts were significantly decreased in wounds of rats treated with AZM, ZnO, or AZM-ZnONPs after three and seven days of infection compared to the control group. However, the reduction in bacterial counts in Group III, which received the AZM-ZnONP formulation, was significantly higher than those achieved when rats were treated by other protocols at three and seven days post infection ($p < 0.01$ and $p < 0.001$, respectively). As expected, Group IV did not show a significant improvement in bacterial levels (Figure 9B).

In addition, the gel containing AZM-loaded ZnO nanoparticles (Group III) showed an increased rate of wound contraction compared to the formulation containing free AZM (Group I). On day 10 post infection, AZM-ZnONPs induced a wound healing of $95.8 \pm 9.8\%$ compared to $71.5 \pm 8.9\%$ in the case of the AZM-treated group or $38.6 \pm 8.1\%$ in the blank group (Group IV) that received non-medicated gel (Figure 9C).
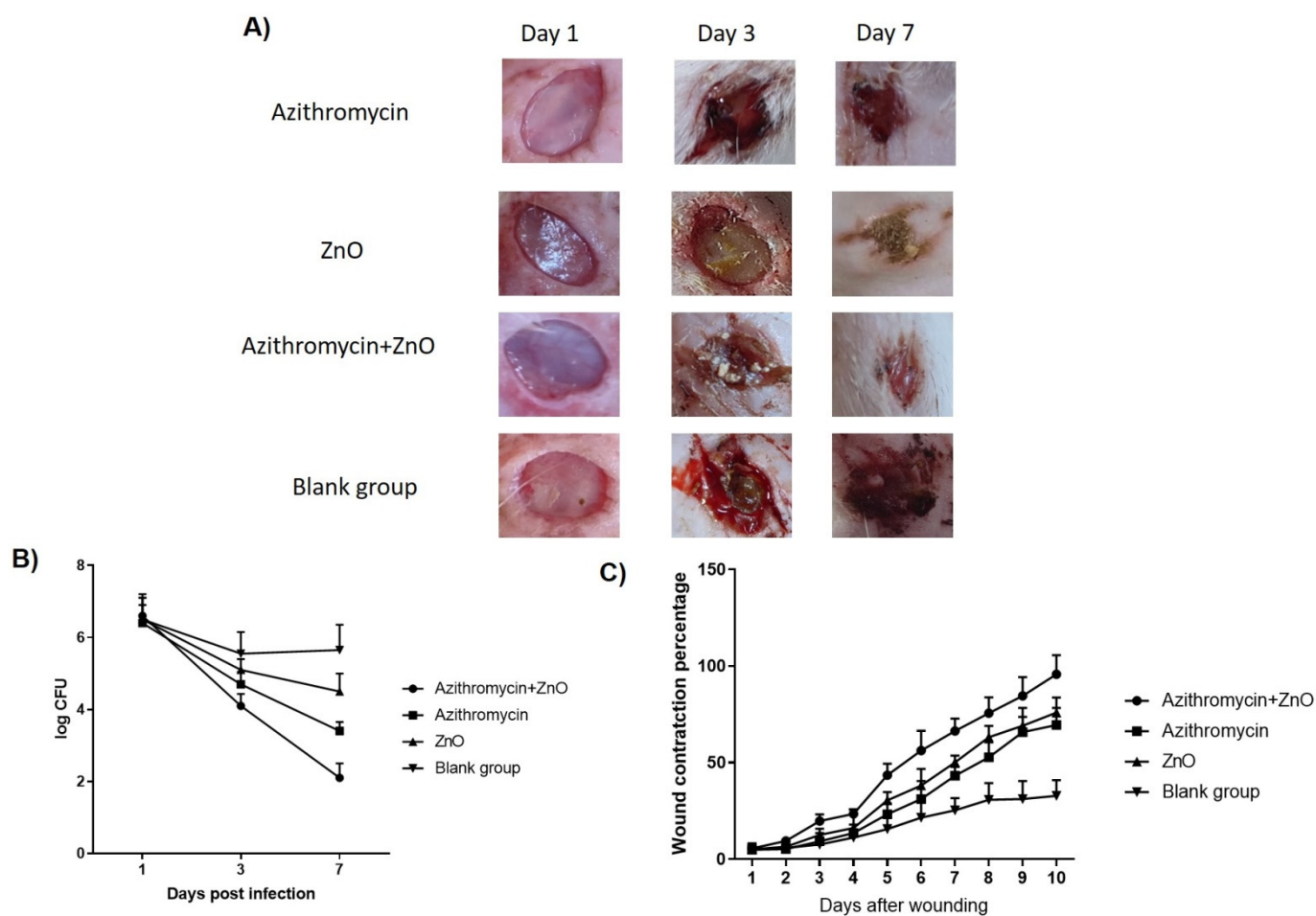
Figure 9. In vivo analysis of the tested preparations. (**A**) Wounds of rats were inoculated with MRSA and treated with indicated preparations then photographed at 1, 3, and 7 days post infection to visualize the healing process. (**B**) Bacterial load burden was evaluated in the wounded skin at 1, 3, and 7 days post infection. The results are expressed as the means ± SD. CFU, colony forming units. (**C**) Effect of AZM, ZnO, and AZM-ZnONPs on the percentage of wound contraction was evaluated over a duration of 10 days after infection.

Antibacterial activities of zinc oxide nanoparticles and AZM has received significant global interest particularly via the application of nanotechnology to develop particles in the nanometer range. According to our results, the combination of AZM and ZnONPs resulted in improved antimicrobial and wound-healing potencies, which may have resulted from the enhanced physicochemical characteristics of the formulation. Analyzing the MIC of the different formulations showed that the AZM-ZnONP formulation was very effective against both MRSA and *E. coli* and the MIC was reduced markedly compared to each of them when used alone. Similarly, Aljihani, et al. [48] reported that liposomal AZM and liposomal AZM/N-acetyl cysteine markedly improved the MIC of AZM against *E. coli*. Another study showed that AZM nanoparticles produced the same inhibitory effect against *E. coli* at an eight times lower concentration compared to free AZM [70]. In another approach, cefixim and AZM were synthesized by anti-solvent precipitation and the synthesized nanoparticles showed better antibacterial activities against *S. aureus*, *E. coli*, Salmonella typhi, and Shigella as tested by agar diffusion assays than the parental drugs [71]. Furthermore, PLGA-loaded AZM nanoparticles had improved antibacterial potential for treating intracellular infections compared to free drugs [72]. Of note, ZnONPs have attractive antimicrobial activities that encourage their use as a therapeutic antimicrobial agent [73]. ZnO can induce bacterial death and/or inhibition through different mechanisms [74]. ZnO can directly interfere with bacterial cell integrity [75], induce the release of antimicrobial

Zn^{+2} ions [76], and generate several reactive oxygen species such as hydrogen peroxide, hydroxyl, and superoxide free radicles, which penetrate the bacterial membranes, leading to bacterial damage and death [77–79]. Furthermore, ZnO nanoparticles may reduce bacterial attachment to biomedical surfaces [80]. Importantly, the combination of ZnO nanoparticles with other antibiotics can lead to enhanced antimicrobial properties, leading to a lower rate of bacterial resistance, shorter treatment durations, and lower drug concentrations used in treatment [81]. Venubabu Thati, et al. [82] noted that ZnO nanoparticles showed better antimicrobial properties when used in combination with other antibiotics such as cephalosporins and aminoglycosides.

3.9. Histological Analysis of the Skin Layers Treated with the Different Formulations

H&E-stained section examination of un-injured animals (negative control group) revealed that the skin consisted of the normal epidermis and the dermis. The epidermis was made up of four layers of stratified keratinized squamous epithelium: stratum basale, stratum spinosum, stratum granulosum, and stratum corneum [83]. Epidermal invaginations were interdigitated with dermal papillae to create the dermal–epidermal junction (DED). The dermis was made up of two layers: an exterior reticular layer rich in collagen, elastic fibers, and connective tissue cells, and an inner reticular layer rich in collagen, elastic fibers, and connective tissue cells (Figure 10a). In the untreated control group, the epidermis showed a significant reduction in thickness compared with group I, in addition to flattening of the dermal–epidermal junction (Figure 10b). Most epidermal cells showed vacuolated cytoplasm and darkly stained nuclei (Figure 10b). However, rats treated with AZM-ZnONPs showed an increased thickness of nucleated keratinocytes. Dermal papillae became deeper and more frequent (Figure 10c,d). Many keratinocytes appear with normal cytoplasm and were not vacuolated, whereas in AZM-ZnONP treatment, more improvement was noticed in the form of retaining the dermal thickness, and most of the cells appeared similar to those of the negative control group (Figure 10e).

With respect to the epidermal thickness, a significant decrease in the skin epidermal thickness was observed in the untreated group. However, rats that received the AZM-ZnONP formulation achieved the highest improvement in epidermal thickness compared to animals that were treated with either AZM or ZnO (Figure 10f).

Furthermore, negative control sections stained with Masson's trichrome revealed copious thick collagen bundles in both the papillary and reticular dermis (Figure 11a). Fine collagen fibers with larger interspaces were seen in the papillary layer of the dermis in the untreated control group. Collagen bundles were also disorganized, and congested blood vessels were observed. In AZM- and ZnO-treated rats, there was a slight increase in the level of collagen fibers. However, in the AZM-ZnONP-treated group, the collagen fibers appeared in normal form and distribution (Figure 11a–e). Regarding the dermal measurements, the percentages of collagen fibers were significantly improved upon treatment. However, the highest levels of collagen fibers were achieved in the AZM-ZnONP-treated group (Figure 11f).
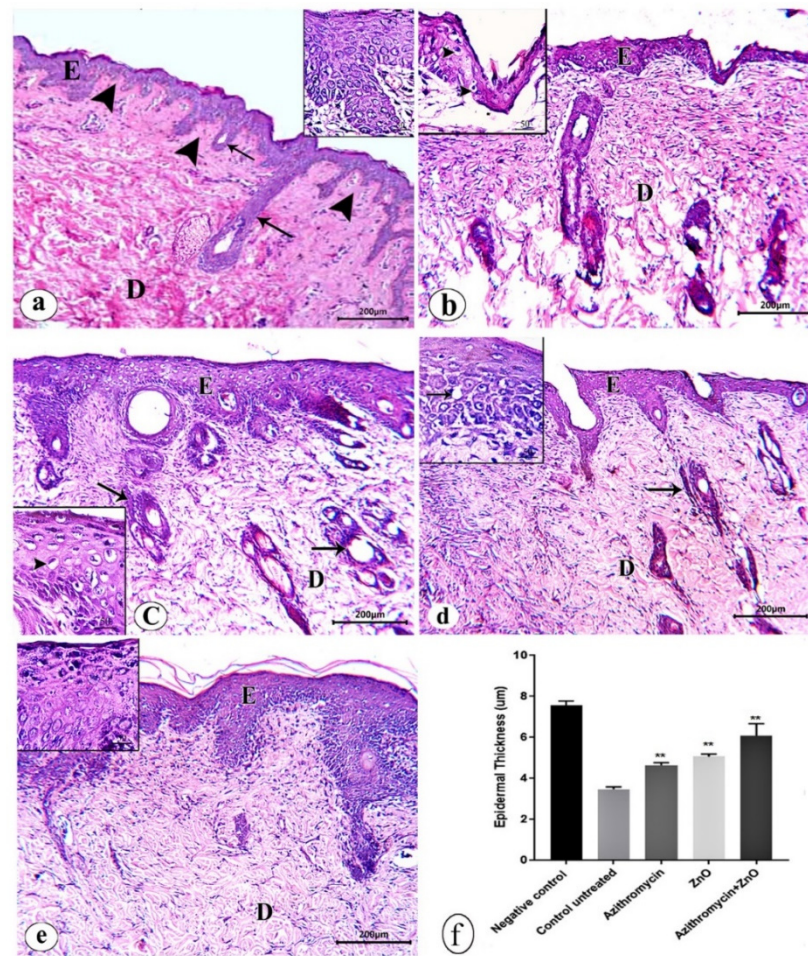
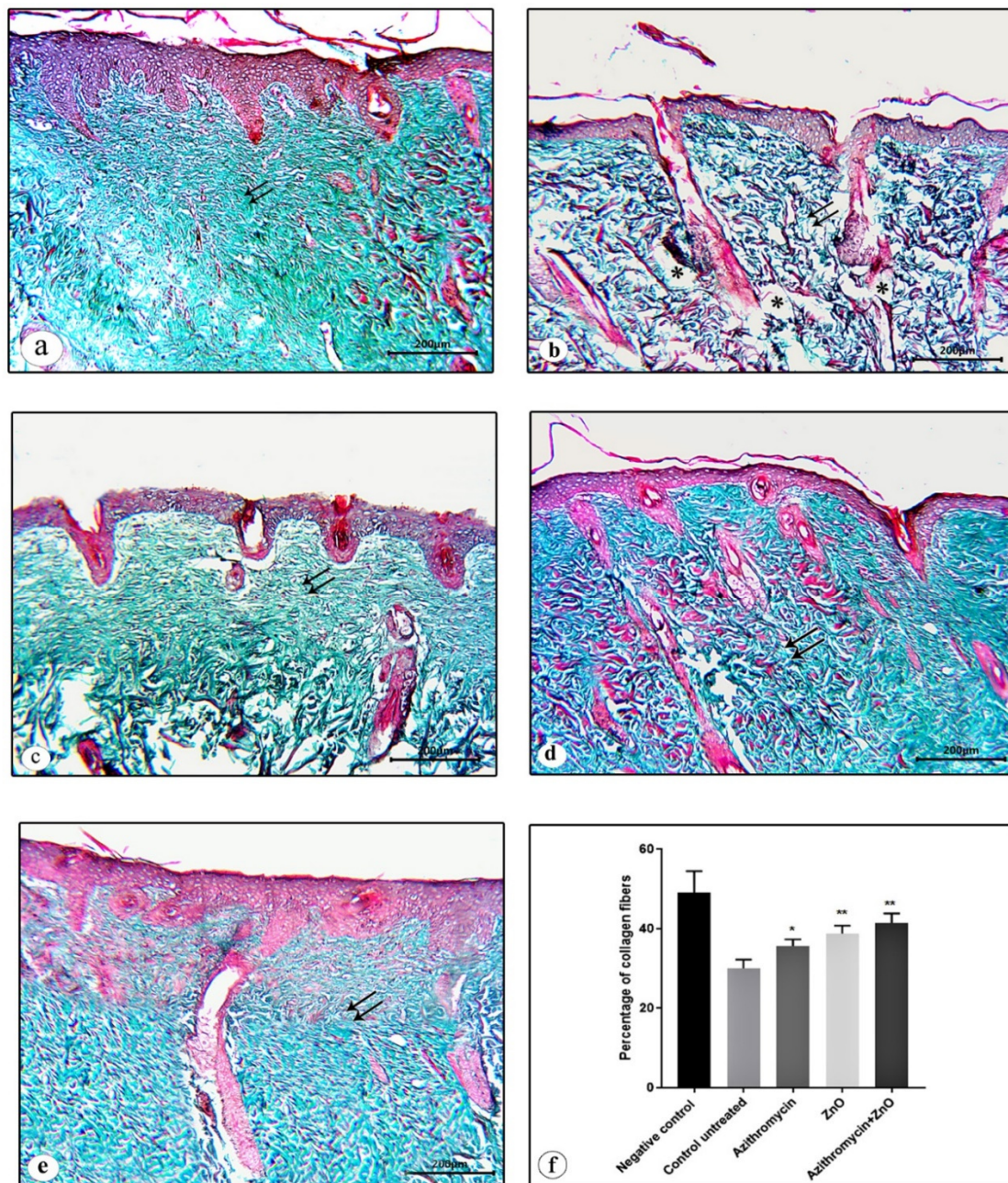**Figure 10.** Hematoxylin-and-eosin-stained sections of skin from rats from all groups. (**a**) Negative control group, (**b**) untreated control group, (**c**) AZM-treated group, (**d**) zinc oxide-treated group, (**e**) AZM-ZnONP-treated group, and (**f**) mean epidermal thickness of skin in different groups. Data are expressed as mean $\pm$ SD. *p*-values were calculated with the Mann–Whitney test. ** *p* value < 0.005. Insets represent magnified sections. Epidermis (E), dermis (D), dermal–epidermal junction (arrowhead), and hair follicles (arrow).

Figure 11. Masson's trichrome-stained sections of skin from rats from all groups. (**a**) Negative control group, (**b**) untreated control group, (**c**) AZM-treated group, (**d**) zinc oxide-treated group, (**e**) AZM-ZnONP-treated group, and (**f**) mean percentage of collagen fibers of dermis in different groups. Data are expressed as mean $\pm$ SD. *p*-values were calculated with the Mann–Whitney test. * *p* value < 0.05. ** *p* value < 0.005. Double arrows refer to collagen fibers.

4. Conclusions

ZnONPs loaded with AZM provided a topical formulation that could markedly promote wound healing of infected wounds. Optimization of the formulation variables was beneficial in the selection of the most effective formula. The loading of AZM onto the surface of ZnONPs provided a healing effect that exceeded the healing effect of either drug alone. The observed in vitro and in vivo antibacterial and wound-healing activities for AZM-ZnONP-treated animals indicates that the developed formulation can offer a better alternative for the treatment of skin infections caused by resistant bacteria. Future studies

will focus on testing the clinical efficacy of AZM-ZnONPs in the treatment of chronic diabetic wounds.

Supplementary Materials: The following are available online at https://www.mdpi.com/article/10.3390/pharmaceutics14010111/s1. Table S1. X-ray data of the prepared ZnO nanoparticles.

References

1. Velnar, T.; Bailey, T.; Smrkolj, V. The wound healing process: An overview of the cellular and molecular mechanisms. *J. Int. Med. Res.* **2009**, *37*, 1528–1542. [CrossRef] [PubMed]
2. WYNN, M. The impact of infection on the four stages of acute wound healing: An overview. *Wounds UK* **2021**, *17*, 26–32.
3. Teaima, M.H.; Elasaly, M.K.; Omar, S.A.; El-Nabarawi, M.A.; Shoueir, K.R. Wound healing activities of polyurethane modified chitosan nanofibers loaded with different concentrations of linezolid in an experimental model of diabetes. *J. Drug Deliv. Sci. Technol.* **2021**. [CrossRef]
4. Fathi, H.A.; Abdelkader, A.; AbdelKarim, M.S.; Abdelaziz, A.A.; El-Mokhtar, M.A.; Allam, A.; Fetih, G.; El Badry, M.; Elsabahy, M. Electrospun vancomycin-loaded nanofibers for management of methicillin-resistant Staphylococcus aureus-induced skin infections. *Int. J. Pharm.* **2020**, *586*, 119620. [CrossRef] [PubMed]
5. Al-Hakkani, M.F.; Gouda, G.A.; Hassan, S.H.A. A review of green methods for phytofabrication of hematite (α-Fe$_2$O$_3$) nanoparticles and their characterization, properties, and applications. *Heliyon* **2021**, *7*, e05806. [CrossRef]
6. Al-Hakkani, M.F. Biogenic copper nanoparticles and their applications: A review. *SN App. Sci.* **2020**, *2*, 505. [CrossRef]
7. Mekkawy, A.I.; El-Mokhtar, M.A.; El-Shanawany, S.M.; Ibrahim, E.H. Silver nanoparticles-loaded hydrogels, a potential treatment for resistant bacterial infection and wound healing: A review. *J. Pharm. Res. Int.* **2016**, *14*, 1–19. [CrossRef]
8. Shkodenko, L.; Kassirov, I.; Koshel, E. Metal oxide nanoparticles against bacterial biofilms: Perspectives and limitations. *Microorganisms* **2020**, *8*, 1545. [CrossRef] [PubMed]
9. Lange, A.; Grzenia, A.; Wierzbicki, M.; Strojny-Cieslak, B.; Kalińska, A.; Gołębiewski, M.; Radzikowski, D.; Sawosz, E.; Jaworski, S. Silver and Copper Nanoparticles Inhibit Biofilm Formation by Mastitis Pathogens. *Animals* **2021**, *11*, 1884. [CrossRef]
10. Khater, M.; Khater, S.S.; Gholap, H.; Patil, R.; Kulkarni, G. Comparative studies on measurement of membrane potential of bacterial cells treated with ZnO nanoparticles by spectrofluorometry, fluorescence microscopy and flowcytometry. *J. Microb. Meth.* **2020**, *173*, 105920. [CrossRef]
11. Mohapatra, S.S.; Limayem, A. Chitosan Oligomer and Zinc Oxide Nanoparticle Compositions for Treating Drug Resistant Bacteria and Biofilm. U.S. Patent 10,675,301, 9 June 2020.
12. Holmes, A.M.; Kempson, I.; Turnbull, T.; Paterson, D.; Roberts, M.S. Penetration of zinc into human skin after topical application of nano zinc oxide used in commercial sunscreen formulations. *ACS Appl. Bio Mater.* **2020**, *3*, 3640–3647. [CrossRef]
13. Abebe, B.; Zereffa, E.A.; Tadesse, A.; Murthy, H.A. A review on enhancing the antibacterial activity of ZnO: Mechanisms and microscopic investigation. *Nanos. Res. Lett.* **2020**, *15*, 190. [CrossRef] [PubMed]
14. Parvinzadeh Gashti, M.; Helali, M.; Karimi, S. Biomineralization-Inspired Green Synthesis of Zinc Phosphate-Based Nanosheets in Gelatin Hydrogel. *Int. J. Appl. Ceram. Technol.* **2016**, *13*, 1069–1073. [CrossRef]
15. Vidya, C.; Hiremath, S.; Chandraprabha, M.; Antonyraj, M.L.; Gopal, I.V.; Jain, A.; Bansal, K. Green synthesis of ZnO nanoparticles by Calotropis gigantea. *Int. J. Curr. Eng. Technol.* **2013**, *1*, 118–120.

16. Aladpoosh, R.; Montazer, M. The role of cellulosic chains of cotton in biosynthesis of ZnO nanorods producing multifunctional properties: Mechanism, characterizations and features. *Carb. Polym.* **2015**, *126*, 122–129. [CrossRef]

17. Krupa, A.N.D.; Vimala, R. Evaluation of tetraethoxysilane (TEOS) sol–gel coatings, modified with green synthesized zinc oxide nanoparticles for combating microfouling. *Mat. Sci. Engin. C* **2016**, *61*, 728–735. [CrossRef]

18. Elumalai, K.; Velmurugan, S.; Ravi, S.; Kathiravan, V.; Ashokkumar, S. RETRACTED: Green synthesis of zinc oxide nanoparticles using Moringa oleifera leaf extract and evaluation of its antimicrobial activity. *Spectrochim. Acta Part A Mol. Biomol. Spectrosc.* **2015**, *143*, 158–164. [CrossRef]

19. Imamura, Y.; Higashiyama, Y.; Tomono, K.; Izumikawa, K.; Yanagihara, K.; Ohno, H.; Miyazaki, Y.; Hirakata, Y.; Mizuta, Y.; Kadota, J.-i. Azithromycin exhibits bactericidal effects on Pseudomonas aeruginosa through interaction with the outer membrane. *Antimic. Agents Chem.* **2005**, *49*, 1377–1380. [CrossRef] [PubMed]

20. Saddik, M.S.; Alsharif, F.M.; El-Mokhtar, M.A.; Al-Hakkani, M.F.; El-Mahdy, M.M.; Farghaly, H.S.; Abou-Taleb, H.A. Biosynthesis, characterization, and wound-healing activity of phenytoin-loaded Copper nanoparticles. *AAPS PharmSciTech* **2020**, *21*, 175. [CrossRef]

21. Saddik, M.S.; Elsayed, M.M.A.; Abdelkader, M.S.A.; El-Mokhtar, M.A.; Abdel-Aleem, J.A.; Abu-Dief, A.M.; Al-Hakkani, M.F.; Farghaly, H.S.; Abou-Taleb, H.A. Novel Green Biosynthesis of 5-Fluorouracil Chromium Nanoparticles Using Harpullia pendula Extract for Treatment of Colorectal Cancer. *Pharmaceutics* **2021**, *13*, 226. [CrossRef]

22. Al-Hakkani, M.F. A rapid, developed and validated RP-HPLC method for determination of azithromycin. *SN Appl. Sci.* **2019**, *1*, 222. [CrossRef]

23. Al-Hakkani, M.F.; Gouda, G.A.; Hassan, S.H.A.; Farghaly, O.A.; Mohamed, M.M.A. Fully investigation of RP- HPLC analytical method validation parameters for determination of Cefixime traces in the different pharmaceutical dosage forms and urine analysis. *Acta Pharm. Sci.* **2021**, *59*, 631–649. [CrossRef]

24. Al-Hakkani, M.F. HPLC analytical method validation for determination of Cefotaxime in the bulk and finished pharmaceutical dosage form. *Sustain. Chem. Eng.* **2020**, 33–42. [CrossRef]

25. Al-Hakkani, M.F. Guideline of inductively coupled plasma mass spectrometry "ICP–MS": Fundamentals, practices, determination of the limits, quality control, and method validation parameters. *SN Appl. Sci.* **2019**, *1*, 791. [CrossRef]

26. Al-Hakkani, M.F. Forced degradation study with a developed and validated RP-HPLC method for determination of cefpodoxime proxetil in the bulk and finished pharmaceutical products. *J. Iran. Chem. Soc.* **2019**, *16*, 1571–1578. [CrossRef]

27. Elkot, M.; Elsayed, M.; Alaaeldin, E.; Sarhan, H.; Shaykoon, M.S.A.; Elsadek, B. Accelerated stability testing of microcapsulated sorafenib-loaded carbon nanotubes prepared by emulsification/internal gelation method. *Int. J. Pharm. Pharm. Res.* **2019**, *16*, 126–139.

28. Husein, D.Z.; Hassanien, R.; Al-Hakkani, M.F. Green-synthesized copper nano-adsorbent for the removal of pharmaceutical pollutants from real wastewater samples. *Heliyon* **2019**, *5*, e02339. [CrossRef]

29. Langmuir, I. The constitution and fundamental properties of solids and liquids. Part I. Solids. *J. Am. Chem. Soc.* **1916**, *38*, 2221–2295. [CrossRef]

30. Freundlich, H. About adsorption in solutions. *J. Phys. Chem.* **1907**, *57*, 385–470.

31. Temkin, M. Kinetics of ammonia synthesis on promoted iron catalysts. *Acta Physiochim.* **1940**, *12*, 327–356.

32. H Auda, S.; M Ahmed, M.; El-Rasoul, A.; I Saleh, K. Formulation and physicochemical characterization of piroxicam containing polymer films. *Bull. Pharm. Sci. Assiut* **2010**, *33*, 33–42. [CrossRef]

33. M Ahmed, M.; H Auda, S.; El-Rasoul, A.; I Saleh, K.; M Zayed, G. Preparation and Evaluation of Diclofenac Sodium–Cellulose Acetate Microcapsules Using Solvent Evaporation Technique. *Bull. Pharm. Sci. Assiut* **2010**, *33*, 43–49. [CrossRef]

34. El-Mahdy, M.; Mohamed, E.-E.M.; Saddik, M.S.; Ali, M.F.; El-Sayed, A.M. Formulation and clinical evaluation of niosomal methylene blue for successful treatment of acne. *J. Adv. Biomed. Pharm. Sci.* **2020**, *3*, 116–126. [CrossRef]

35. Saddik, M.S.; Mohamed, E.; Elmahdy, M.M. Preparation and Characterization of Niosomal Carrier System of Hydrophilic Drug (Methylene Blue) for Photodynamic Therapy. *Lat. Am. J. Pharm.* **2020**, *39*, 561–569.

36. Auda, S.H.; Abd El-Rasoul, S.; Ahmed, M.M.; Osman, S.K.; El-Badry, M. In-vitro release and in-vivo performance of tolmetin from different topical gel formulations. *J. Pharm. Innov.* **2015**, *45*, 311–317. [CrossRef]

37. Abd El Rasoul, S.; Saleh, K. Emulsion solvent evaporation method for preparing Eudragit RS100 microparticles loaded ketorolac tromethamine. *Asian J. Pharm. Health Sci.* **2013**, *3*, 627–639.

38. Ahmed, M.M. Effect of different formulation variables on release characteristics of gastro-floating microspheres of ethyl cellulose/carbopol 934P encapsulating sorafenib. *Int. J. Pharm. Pharm. Sci.* **2019**, *11*, 64–70. [CrossRef]

39. Ahmed, M.M.; Abd El-Rasoul, S.; Auda, S.H.; Ibrahim, M.A. Emulsification/internal gelation as a method for preparation of diclofenac sodium–sodium alginate microparticles. *Saudi Pharm. J.* **2013**, *21*, 61–69. [CrossRef]

40. Refaat, H.; Naguib, Y.W.; Elsayed, M.; Sarhan, H.A.; Alaaeldin, E. Modified spraying technique and response surface methodology for the preparation and optimization of propolis liposomes of enhanced anti-proliferative activity against human melanoma cell line A375. *Pharmaceutics* **2019**, *11*, 558. [CrossRef] [PubMed]

41. Tawfeek, H.M.; Abdel-Aleem, J.A.; Ahmed, M.M. Development and optimization of itopride hydrochloride fast disintegrating tablets using factorial design and response surface methodology. *Intern. J. Pharm. Sci. Res.* **2015**, *6*, 1661.

42. Elsayed, M. Controlled release alginate-chitosan microspheres of tolmetin sodium prepared by internal gelation technique and characterized by response surface modeling. *Braz. J. Pharm. Sci.* **2021**, *56*. [CrossRef]

43. Elsayed, M.; Okda, T.M.; Atwa, G.M.; Omran, G.A.; Abd Elbaky, A.E. Design and Optimization of Orally Administered Luteolin Nanoethosomes to Enhance Its Anti-Tumor Activity against Hepatocellular Carcinoma. *Pharmaceutics* **2021**, *13*, 648. [CrossRef]

44. Elsayed, M.M.; Abd El Rasoul, S.; Hussein, A.K. Response surface methodology as a useful tool for development and optimization of sustained release ketorolac tromethamine niosomal organogels. *J. Pharm. Innov.* **2019**, *15*, 664–677. [CrossRef]

45. El-Shenawy, A.A.; Ahmed, M.M.; Mansour, H.F.; Abd El Rasoul, S. Torsemide fast dissolving tablets: Development, optimization using Box–Bhenken design and response surface methodology, in vitro characterization, and pharmacokinetic assessment. *AAPS PharmSciTech* **2017**, *18*, 2168–2179. [CrossRef] [PubMed]

46. Allam, A.; El-Mokhtar, M.A.; Elsabahy, M. Vancomycin-loaded niosomes integrated within pH-sensitive in-situ forming gel for treatment of ocular infections while minimizing drug irritation. *J. Pharm. Pharm.* **2019**, *71*, 1209–1221. [CrossRef]

47. Hetta, H.F.; Al-Kadmy, I.M.S.; Khazaal, S.S.; Abbas, S.; Suhail, A.; El-Mokhtar, M.A.; Ellah, N.H.A.; Ahmed, E.A.; Abd-Ellatief, R.B.; El-Masry, E.A.; et al. Antibiofilm and antivirulence potential of silver nanoparticles against multidrug-resistant Acinetobacter baumannii. *Sci. Rep.* **2021**, *11*, 10751. [CrossRef] [PubMed]

48. Aljihani, S.A.; Alehaideb, Z.; Alarfaj, R.E.; Alghoribi, M.F.; Akiel, M.A.; Alenazi, T.H.; Al-Fahad, A.J.; Al Tamimi, S.M.; Albakr, T.M.; Alshehri, A.; et al. Enhancing azithromycin antibacterial activity by encapsulation in liposomes/liposomal-N-acetylcysteine formulations against resistant clinical strains of Escherichia coli. *Saudi J. Biol. Sci.* **2020**, *27*, 3065–3071. [CrossRef] [PubMed]

49. Mekkawy, A.I.; El-Mokhtar, M.A.; Nafady, N.A.; Yousef, N.; Hamad, M.A.; El-Shanawany, S.M.; Ibrahim, E.H.; Elsabahy, M. In vitro and in vivo evaluation of biologically synthesized silver nanoparticles for topical applications: Effect of surface coating and loading into hydrogels. *J. Nanomed.* **2017**, *12*, 759. [CrossRef]

50. Clark, J.D.; Gebhart, G.F.; Gonder, J.C.; Keeling, M.E.; Kohn, D.F. The 1996 guide for the care and use of laboratory animals. *J. ILAR J.* **1997**, *38*, 41–48. [CrossRef]

51. Zeng, Q.; Xie, H.; Song, H.; Nie, F.; Wang, J.; Chen, D.; Wang, F. In Vivo Wound Healing Activity of Abrus cantoniensis Extract. *Evid. Based Complem. Alternat. Med.* **2016**, *2016*, 6568528. [CrossRef]

52. Kömüves, L.G.; Hanley, K.; Man, M.-Q.; Elias, P.M.; Williams, M.L.; Feingold, K.R. Keratinocyte differentiation in hyperproliferative epidermis: Topical application of PPARα activators restores tissue homeostasis. *J. Investig. Dermatol.* **2000**, *115*, 361–367. [CrossRef]

53. Elsayed, M.M.; Mostafa, M.E.; Alaaeldin, E.; Sarhan, H.A.; Shaykoon, M.S.; Allam, S.; Ahmed, A.R.; Elsadek, B.E. Design and characterisation of novel Sorafenib-loaded carbon nanotubes with distinct tumour-suppressive activity in hepatocellular carcinoma. *Intern. J. Nanomed.* **2019**, *14*, 8445. [CrossRef]

54. Khan, S.B.; Faisal, M.; Rahman, M.M.; Jamal, A. Low-temperature growth of ZnO nanoparticles: Photocatalyst and acetone sensor. *Talanta* **2011**, *85*, 943–949. [CrossRef] [PubMed]

55. Chithra, M.J.; Sathya, M.; Pushpanathan, K. Effect of pH on crystal size and photoluminescence property of ZnO nanoparticles prepared by chemical precipitation method. *Acta Metall. Sin. (Engl. Lett.)* **2015**, *28*, 394–404. [CrossRef]

56. Mesaros, A.; Ghitulica, C.D.; Popa, M.; Mereu, R.; Popa, A.; Petrisor Jr, T.; Gabor, M.; Cadis, A.I.; Vasile, B.S. Synthesis, structural and morphological characteristics, magnetic and optical properties of Co doped ZnO nanoparticles. *Ceram. Int.* **2014**, *40*, 2835–2846. [CrossRef]

57. Al-Hakkani, M.F.; Hassan, S.H.A.; Saddik, M.S.; El-Mokhtar, M.A.; Al-Shelkamy, S.A. Bioengineering, characterization, and biological activities of C@Cu$_2$O@Cu nanocomposite based-mediated the *Vicia faba* seeds aqueous extract. *J. Mater. Res. Technol.* **2021**, *14*, 1998–2016. [CrossRef]

58. Al-Hakkani, M.F.; Gouda, G.A.; Hassan, S.H.A.; Nagiub, A.M. *Echinacea purpurea* mediated hematite nanoparticles (α-HNPs) biofabrication, characterization, physicochemical properties, and its in-vitro biocompatibility evaluation. *Surf. Interf.* **2021**, *24*, 101113. [CrossRef]

59. Robaina, N.F.; de Paula, C.E.R.; Brum, D.M.; de la Guardia, M.; Garrigues, S.; Cassella, R.J. Novel approach for the determination of azithromycin in pharmaceutical formulations by Fourier transform infrared spectroscopy in film-through transmission mode. *Microchem. J.* **2013**, *110*, 301–307. [CrossRef]

60. Abu-Dief, A.M.; Abdelbaky, M.S.; Martínez-Blanco, D.; Amghouz, Z.; García-Granda, S. Effect of chromium substitution on the structural and magnetic properties of nanocrystalline zinc ferrite. *Mater. Chem. Phys.* **2016**, *174*, 164–171. [CrossRef]

61. Ali, M.A.E.A.A.; Abu-Dief, A.M. CuFe$_2$O$_4$ nanoparticles: An efficient heterogeneous magnetically separable catalyst for synthesis of some novel propynyl-1H-imidazoles derivatives. *Tetrahedron* **2015**, *71*, 2579–2584.

62. Abdel-Rahman, L.H.; Abu-Dief, A.M.; El-Khatib, R.M.; Abdel-Fatah, S.M. Some new nano-sized Fe (II), Cd (II) and Zn (II) Schiff base complexes as precursor for metal oxides: Sonochemical synthesis, characterization, DNA interaction, in vitro antimicrobial and anticancer activities. *Bioorg. Chem.* **2016**, *69*, 140–152. [CrossRef]

63. Abdel-Rahman, L.H.; Abu-Dief, A.M.; El-Khatib, R.M.; Abdel-Fatah, S.M. Sonochemical synthesis, DNA binding, antimicrobial evaluation and in vitro anticancer activity of three new nano-sized Cu (II), Co (II) and Ni (II) chelates based on tri-dentate NOO imine ligands as precursors for metal oxides. *J. Photochem. Photobiol. B Biol.* **2016**, *162*, 298–308. [CrossRef] [PubMed]

64. Abdel-Rahman, L.H.; Abu-Dief, A.M.; Adam, M.S.S.; Hamdan, S.K. Some new nano-sized mononuclear Cu (II) Schiff base complexes: Design, characterization, molecular modeling and catalytic potentials in benzyl alcohol oxidation. *Catal. Lett.* **2016**, *146*, 1373–1396. [CrossRef]

65. Aleem Ali El-Remaily, M.A.E.; Abu-Dief, A.M.; El-Khatib, R.M. A robust synthesis and characterization of superparamagnetic CoFe$_2$O$_4$ nanoparticles as an efficient and reusable catalyst for green synthesis of some heterocyclic rings. *Appl. Organ. Chem.* **2016**, *30*, 1022–1029. [CrossRef]

66. Esmaeili Bidhendi, M.; Poursorkh, Z.; Sereshti, H.; Rashidi Nodeh, H.; Rezania, S.; Afzal Kamboh, M. Nano-Size Biomass Derived from Pomegranate Peel for Enhanced Removal of Cefixime Antibiotic from Aqueous Media: Kinetic, Equilibrium and Thermodynamic Study. *Int. J. Environ. Res. Public Health* **2020**, *17*, 4223. [CrossRef] [PubMed]

67. Rukavina, Z.; Klarić, M.Š.; Filipović-Grčić, J.; Lovrić, J.; Vanić, Ž. Azithromycin-loaded liposomes for enhanced topical treatment of methicillin-resistant Staphyloccocus aureus (MRSA) infections. *Int. J Pharm.* **2018**, *553*, 109–119. [CrossRef]

68. El-Rasoul, A.; Ahmed, M.M. Chitosan polymer as a coat of calcium alginate microcapsules loaded by non-steroidal antiinflammatory drug. *Bull. Pharm. Sci. Assiut* **2010**, *33*, 179–186. [CrossRef]

69. Elsayed, M. Design and optimization of tolmetin sodium microspheres prepared by emulsification-internal gelation using response surface methodology. *Al-Azh J. Pharm. Sci.* **2012**, *45*, 383–398. [CrossRef]

70. Azhdarzadeh, M.; Lotfipour, F.; Zakeri-Milani, P.; Mohammadi, G.; Valizadeh, H. Anti-bacterial performance of azithromycin nanoparticles as colloidal drug delivery system against different gram-negative and gram-positive bacteria. *J. Adv. Pharm. Bull.* **2012**, *2*, 17.

71. Khan, F.A.; Zahoor, M.; Islam, N.U.; Hameed, R. Synthesis of cefixime and azithromycin nanoparticles: An attempt to enhance their antimicrobial activity and dissolution rate. *J. Nanomater.* **2016**, *2016*, 6909085. [CrossRef]

72. Mohammadi, G.; Valizadeh, H.; Barzegar-Jalali, M.; Lotfipour, F.; Adibkia, K.; Milani, M.; Azhdarzadeh, M.; Kiafar, F.; Nokhodchi, A. Development of azithromycin–PLGA nanoparticles: Physicochemical characterization and antibacterial effect against Salmonella typhi. *J. Coll. Surf. B Biointerf.* **2010**, *80*, 34–39. [CrossRef] [PubMed]

73. Abo-Shama, U.H.; El-Gendy, H.; Mousa, W.S.; Hamouda, R.A.; Yousuf, W.E.; Hetta, H.F.; Abdeen, E.E. Synergistic and antagonistic effects of metal nanoparticles in combination with antibiotics against some reference strains of pathogenic microorganisms. *J. Infect. Drug Resist.* **2020**, *13*, 351. [CrossRef] [PubMed]

74. Sirelkhatim, A.; Mahmud, S.; Seeni, A.; Kaus, N.H.M.; Ann, L.C.; Bakhori, S.K.M.; Hasan, H.; Mohamad, D. Review on Zinc Oxide Nanoparticles: Antibacterial Activity and Toxicity Mechanism. *Nanomicro. Lett.* **2015**, *7*, 219–242. [CrossRef]

75. Zhang, L.; Jiang, Y.; Ding, Y.; Povey, M.; York, D. Investigation into the antibacterial behaviour of suspensions of ZnO nanoparticles (ZnO nanofluids). *J. Nanopart. Res.* **2007**, *9*, 479–489. [CrossRef]

76. Li, M.; Zhu, L.; Lin, D. Toxicity of ZnO nanoparticles to Escherichia coli: Mechanism and the influence of medium components. *Environ. Sci. Technol.* **2011**, *45*, 1977–1983. [CrossRef]

77. Sawai, J.; Shoji, S.; Igarashi, H.; Hashimoto, A.; Kokugan, T.; Shimizu, M.; Kojima, H. Hydrogen peroxide as an antibacterial factor in zinc oxide powder slurry. *J. Ferment. Bioeng.* **1998**, *86*, 521–522. [CrossRef]

78. Kairyte, K.; Kadys, A.; Luksiene, Z. Antibacterial and antifungal activity of photoactivated ZnO nanoparticles in suspension. *J. Photochem. Photobiol. B* **2013**, *128*, 78–84. [CrossRef]

79. Lipovsky, A.; Nitzan, Y.; Gedanken, A.; Lubart, R. Antifungal activity of ZnO nanoparticles–the role of ROS mediated cell injury. *Nanotechnology* **2011**, *22*, 105101. [CrossRef]

80. Yamamoto, O. Influence of particle size on the antibacterial activity of zinc oxide. *Int. J. Inorg. Mat.* **2001**, *3*, 643–646. [CrossRef]

81. Hwang, I.-s.; Hwang, J.H.; Choi, H.; Kim, K.-J.; Lee, D.G. Synergistic effects between silver nanoparticles and antibiotics and the mechanisms involved. *J. Med. Microb.* **2012**, *61*, 1719–1726. [CrossRef]

82. Venubabu Thati, A.; Roy, S.; Prasad, M.A.; Shivannavar, C.; Gaddad, S. Nanostructured zinc oxide enhances the activity of antibiotics against Staphylococcus aureus. *J. Biosci. Technol.* **2010**, *1*, 64–69.

83. Elnaggar, Y.S.; El-Refaie, W.M.; El-Massik, M.A.; Abdallah, O.Y. Lecithin-based nanostructured gels for skin delivery: An update on state of art and recent applications. *J. Control. Release* **2014**, *180*, 10–24. [CrossRef] [PubMed]